MAPPING AREAS IMPACTED BY VOLCANIC FLOWS DURING AN ERUPTION USING SYNTHETIC APERTURE RADAR AND OPTICAL IMAGERY

E. Macorps[1,*], M. Jo[1,2], B. Osmanoglu[1], R. A. Albayrak[1,2]
[1] NASA Goddard Space Flight Center, Greenbelt, MD, USA – (elodie.macorps, minjeong.jo, batuhan.osmanoglu)@nasa.gov
[2] University of Maryland, Baltimore County, MD, USA – albayrak@umbc.edu

KEY WORDS: SAR, NDVI, Disasters Mapping, Volcanic Flows, Surface Roughness

ABSTRACT:

During volcanic disasters, the remoteness of the terrains combined with potentially incapacitated lifelines (e.g., disturbed transportation network) prevent ground-based surveys for timely assessment of damage extents. To that effect, we worked to combine satellite optical and Synthetic Aperture Radar (SAR) data to rapidly delineate the areas impacted by fast-moving volcanic flows during an eruption (e.g., Pyroclastic Density Currents (PDCs), lahars), which can in turn be used to target and organize the response efforts. We used the 2015 eruptions of Volcán de Colima (Mexico) and Volcán Calbuco (Chile) volcanoes to calibrate detection thresholds of different types of volcanic flows, from optical and SAR imagery. Optical imagery is used to calculate temporal changes of Normalized Difference Vegetation Index (NDVI) associated with the presence of erupted materials on the surface. SAR amplitude images are used to detect changes in surface roughness (sigma0) attributed to the emplacement of new volcanic flows. Classification of the respective NDVI and SAR amplitude signal changes for different types of volcanic flows is done using very-high-resolution imagery and ground-based data obtained during field work. Linear rescaling of minimal and maximal threshold signals is used to create probability maps of volcanic flow deposits extent, and then combined into a joint probability map to maximize the accuracy of the deposit extents. We tested our ability to generate volcanic flow extent maps during the April 2021 eruption of Soufrière St Vincent, using this detection method and the calibrated threshold values for PDCs and lahars.

1. INTRODUCTION

The cost of a disaster, both in terms of economic loss and fatalities, is dependent upon the rapidity and efficacy of the event response. Recent volcanic crises like the 2018 eruptions at Fuego (Guatemala) and Anak Krakatau (Indonesia), which were both responsible for over 430 dead and missing persons according to authorities, are tragic examples of how the lack of monitoring capabilities can have dramatic consequences (Auker et al., 2013; Agencias Guatemalteca de Noticias, 2019). Emergency managers can most benefit from satellite remote sensing tools at active volcanoes where ground-based monitoring and field work are dangerous, and sometimes impossible, due to the remote characteristics of the location, natural hazards (eruptive activity, dense vegetation, and rugged relief) or socio-political reasons (Head et al., 2012). Pre-eruptive monitoring can help improve early warnings, followed by syn-eruptive monitoring to provide critical information for hazard mitigation, and post-eruptive monitoring to support disaster response (Poland, 2015).

Multiple remote sensing sensors, platforms and techniques exist in the framework of emergency mapping, and the choice depends on the type and size of disasters being mapped and details required (Boccardo and Giulio Tonolo, 2014). In this research, we focus on medium-resolution (30-m) mapping of fast-moving volcanic flows (e.g., PDCs and lahars) to support emergency responders with rapid delineation of impacted areas. This is important to establish evacuation routes and target rescue efforts. We contrast this to slow-moving lava flows, which can destroy as many infrastructures and lifelines as the other fast-moving volcanic flows but are easily escapable and rarely directly threaten human lives (Harris, 2015).

Multi-sensor analysis strategically increases the range of detectable surface changes during or shortly after an eruption by providing different temporal and spatial-resolution datasets, all the while alleviating the limitations of each sensor types. For instance, while optical (visible and near-infrared) data can provide direct observations of the areas covered by volcanic flows, they require cloud-free skies, which is often restricted during an eruption due to heavy ash clouds or rain. SAR data, on the other hand, compensate for these limitations with all-weather and all-day imaging capabilities. SAR and optical data have been applied to fast-moving volcanic flows in other studies, either individually (Wadge et al., 2002, 2011; Terunuma et al., 2005; Thouret et al., 2010; Solikhin et al., 2012; Bignami et al., 2013; Arnold et al., 2018; Krippner et al., 2018; Pallister et al., 2019; Valade et al., 2019; Dualeh et al., 2021) or in combination (e.g., Solikhin et al., 2015; McAlpin et al., 2013), but the context of emergency mapping has rarely been a focus.

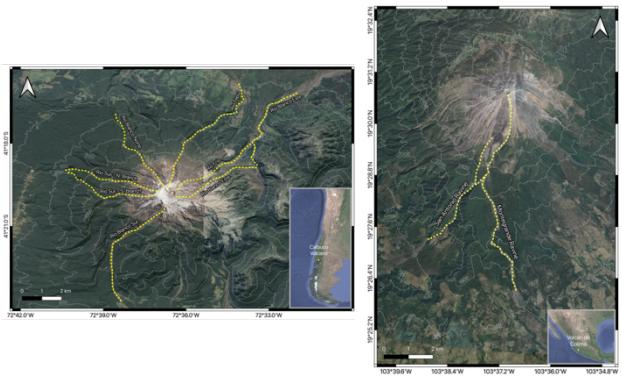

Figure 1. Google Earth maps with topographic contour lines at Volcán Calbuco (left) and Volcán de Colima (right). The valleys in which PDCs were deposited during the 2015 eruptions are highlighted in yellow dashed lines. The inset maps shows the location of both volcanoes, in South and Central America respectively.

* Corresponding author

In this paper, we use the case studies of the 2015 eruptions from Volcán de Colima in Mexico and Volcán Calbuco in Chile (Figure 1) to calibrate detection thresholds of different types of fast-moving volcanic flows from optical and SAR imagery. Surface changes caused by the deposition of PDCs and lahars are measured from differential information between pre- and post-eruption images. Normal Difference Vegetation Index (NDVI) from Landsat-8 OLI images and SAR backscattering intensity changes from ALOS-2 PALSAR images are used in tandem to retrieve the extent of PDCs and lahars. Very high-resolution optical imagery and field-based data are used for validation. The change detection thresholds from NDVI and SAR backscattering intensity are then used in joint probability mapping to refine the delineation of areas impacted by these flows. Finally, we applied the method during a recent volcanic crisis at Soufriere St Vincent.

2. MATERIALS AND METHODS

2.1 Study Sites

2.1.1 Volcán Calbuco (1974 m a.s.l.) located in the Southern Andes of Chile (Figure 1) experienced an abrupt sub-Plinian eruption on the evening of April 22, 2015, after 43 years of quiescence. A first pulsatory ash-rich column, sustained for 90-min, rose up to 15 km (height above crater) in the atmosphere and formed an umbrella cloud expanding and dispersing tephra to the NE. After a 5h30min-break, in the night of April 23, 2015, the second and more violent phase of the eruption began and generated a 6 hour-long sustained eruption plume that reached a maximum height of 28 km, with an umbrella cloud dispersing tephra again to the NE. The partial and eventually complete collapses of the two successive eruption plumes resulted in multiple PDCs that descended into the main drainage pathways around the volcano.
Concurrently, the melting of the summit glacier contributed to the generation of syn- and post-eruption lahars, that were bulking from remobilization of both PDC and tephra deposits. Such secondary lahars can be extremely devastating because they occur after the eruption has ended and can run twice the length of the flows they are eroding. The lack of warning signs and the high intensity of the eruption resulted in significant issues with critical lifelines (blocked roads and destroyed bridges) and evacuations being hindered. Many infrastructures were destroyed by the PDCs, thick accumulation of tephra fall and lahars.

2.1.2 Volcán de Colima (3860 m a.s.l), located at the western end of the Trans-Mexican Volcanic Belt (Figure 1), is one of the most historically active volcanoes in North America. On July 10-11, 2015, Volcán de Colima experienced a significant dome-collapse and partial flank collapse event that sent a series of PDCs onto the southern flank of the volcano into just two main ravines (Macorps et al., 2018). In the following months after the dome-collapse, the rainy season was marked by Hurricane Patricia in October 2015, which contributed to the generation of multiple stream-flows and lahars, cutting into the existing deposits and reworking them to long runout distances. Although the total volume of PDCs at Colima was 10 times lower than that of Calbuco, it was the longest recorded runout distance at Volcán de Colima for a dome-collapse event. This raised the necessity of updating hazard maps accordingly.

2.2 NDVI Change Detection

Optical images from the Operational Land Imager (OLI) sensor of Landsat-8 satellite are used to compute Normalized Difference Vegetation Index (NDVI) values for pre- and post-eruption scenes at Volcán de Colima and Volcán Calbuco using Equation 1:

$$NDVI = \frac{\rho_{NIR} - \rho_R}{\rho_{NIR} + \rho_R}, \quad (1)$$

where: ρ_{NIR} = surface reflectance of band 5 (near-infrared)
ρ_R = surface reflectance of band 4 (red)

Radiometric calibration and atmospheric correction of each Landsat-8 scene is done with the ARCSI Software (Bunting and Clewley, 2018) to remove differences in land surface and atmospheric conditions, as well as solar position and sensor geometry during the different image acquisitions (Lu et al., 2004; Pu et al., 2017). Normalization of pairs of pre- and post-eruption NDVI images is then performed using linear regression of NDVI values for polygons of unchanged land-cover/land-use areas (Pu et al., 2017; Macorps, 2021). This allows to remove seasonal changes of vegetation (i.e., plant phenological stages). Finally, the normalized NDVI image pairs can be used to create absolute NDVI ratio images, hereafter referred to as $|Q_{NDVI}|$, where surface changes caused by the eruption can be detected. The workflow for processing the Landsat-8 OLI bands and producing time-series of normalized pre- over post-eruption NDVI ratio images is presented in Figure 2.

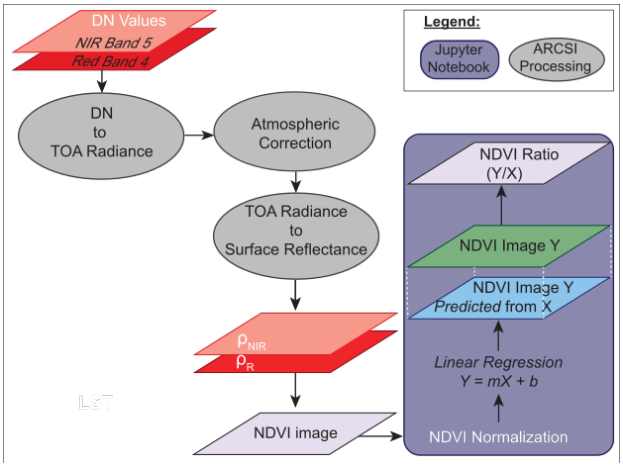

Figure 2. Workflow for processing Landsat-8 bands 4 and 5 for generating pre- over post-eruption $|Q_{NDVI}|$ images

2.3 SAR Backscattering Intensity Change Detection

The SAR dataset consists of ALOS-2 PALSAR images acquired in Fine Beam mode, with dual-polarization (HH and HV) in both ascending and descending orbits for Volcán de Colima, and only in ascending orbit for Volcán Calbuco. The full resolution geocoded backscatter images are produced with the GAMMA software package (Werner and Strozzi, 2000) Finally, the intensity images are converted from linear values to decibels using Equation 2, with ±0.5 dB radiometric accuracy (Motohka et al., 2018):

$$dB = 10 \times log10\,(pwr), \quad (2)$$

where: pwr = linear intensity values
dB = decidbels

SAR backscatter intensity is influenced by the local terrain, including local slope, surface roughness and terrain composition. A smoother surface will produce a weaker backscatter intensity (given the same local slope), thus resulting in a weaker signal

(darker pixels), and vice versa. The water content and surface temperature will also result in different backscatter intensity, particularly for crop fields and growing vegetation. Changes in SAR backscattering intensity, hereafter referred to as ΔdB, are computed from differences between pairs of pre- and post-eruption intensity images, thus showing changes in surface properties.

2.4 Reference Data for Signal Change Classification

The final outlines of the extent of PDCs and lahars for validation is obtained from very high-resolution images and fieldwork data (Macorps et al., 2018; Macorps, 2021). These are used to classify the $|Q_{NDVI}|$ and ΔdB signals corresponding to the emplacement of new volcanic flows during the two eruptions. We use histogram thresholding to compute statistics and classify the detection signals for individual types of volcanic flows.

3. MAPPING OF VOLCANIC FLOWS

3.1 $|Q_{NDVI}|$ and ΔdB Detection Signals

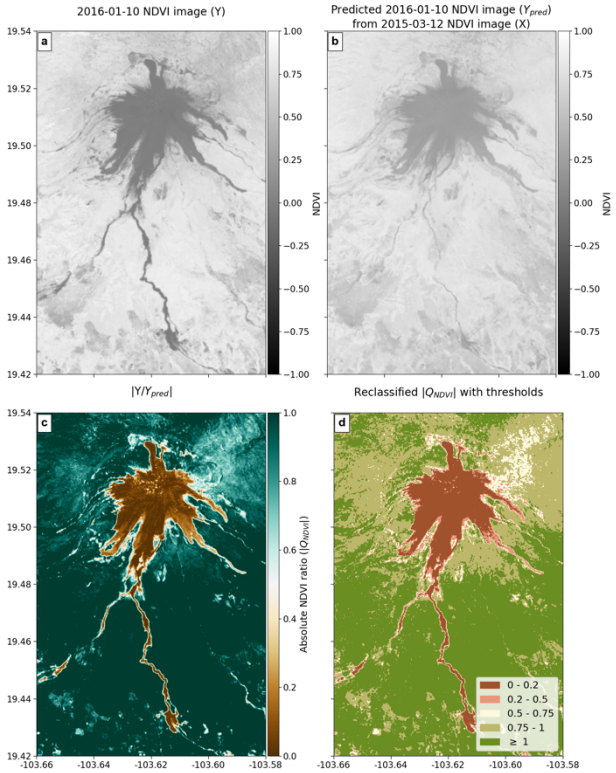

Figure 3. **a)** Post-eruption and **b)** predicted pre-eruption Landsat-8 NDVI images of the southern flank of Volcán de Colima. **c)** $|Q_{NDVI}|$ image obtained from NDVI image (a) divided by (b). **d)** Reclassified $|Q_{NDVI}|$ image with threshold values that emphasize the deposition of new volcanic materials.

High NDVI values represent vegetated surfaces and contrast with bare ground and/or volcanic deposits represented with low NDVI values (Figures 3a,b and 4a,b). Therefore, low $|Q_{NDVI}|$ values can be used to track vegetation removal and deposition of new volcanic flows on the flanks of the volcanoes (Figures 3c and 4c). By reclassifying the $|Q_{NDVI}|$ images using threshold values, we found that the PDCs and lahar deposits have $|Q_{NDVI}| \leq 0.2$ (Figures 3d and 4d). Near the summit, however, where the vegetation is scarce to begin with, it is more difficult to distinguish between different types of volcanic products (e.g., PDCs vs. tephra fall) and to delineate new vs. older materials.

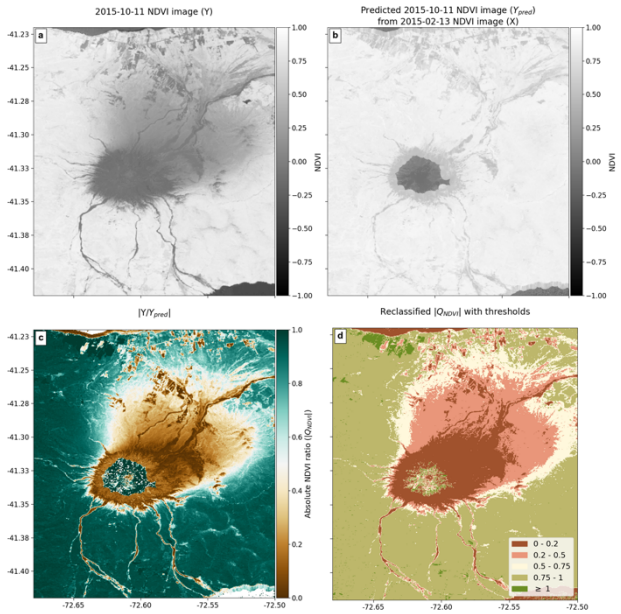

Figure 4. **a)** Post-eruption and **b)** predicted pre-eruption Landsat-8 NDVI images of the southern flank of Volcán Calbuco. **c)** $|Q_{NDVI}|$ image obtained from NDVI image (a) divided by (b). **d)** Reclassified $|Q_{NDVI}|$ image with threshold values that emphasize the deposition of new volcanic materials.

For the detection of SAR backscattering intensity changes, a viewing-friendly method for highlighting the surface changes consists of combining pre-eruption, post-eruption and the ratio of post/pre-eruption in the RGB channels to create a false-color composite image (Figures 5 and 6). The changes in SAR backscattering intensity are associated with changes in surface roughness from the emplacement of new volcanic flows and tephra fall deposits.

On ΔdB images (Figures 7 and 8), $\Delta dB < 0$ values (dark pixels) are detected where PDCs and lahars are deposited because the infilling of the valleys makes the ground smoother on the scale of the radar, thus decreasing the backscattering intensity. On the valley interfluves, the lower magnitude $\Delta dB < 0$ is related to the blanketed topography by thin ash-cloud surge and overbank deposits (i.e., flows that overtopped the valley walls, Macorps et al., 2018), and tephra fall deposits, which often strips the vegetation, making the ground smoother (i.e., removes the contribution of volumetric scattering, hence decreasing the backscatter). The $\Delta dB > 0$ values (brighter pixels) incising through the PDCs deposits are interpreted as erosion and remobilization of deposits by lahars and runoff (Figures 6, 7 and 8). The reworked PDCs and their erosion generate increased surface roughness and can be used to track the occurrence of lahars shortly after the eruption. At Volcán de Colima, the $\Delta dB>0$ values near the summit are caused by increased surface roughness from the emplacement of the post dome-collapse lava flows (Figures 5 and 7). At Volcán Calbuco, the $\Delta dB > 0$ values in the crater/summit area can be explained by increased roughness from crater excavation and by the removal of snow/ice cover (Figure 8).

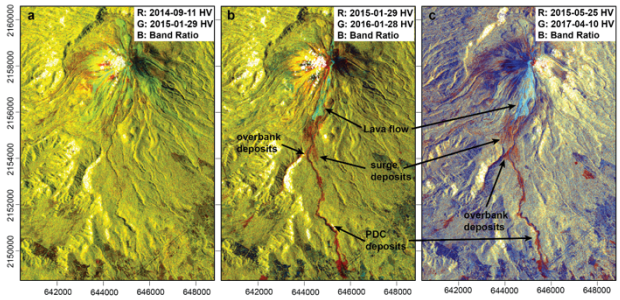

Figure 5. Georeferenced ALOS-2 false-color composite intensity ratio images of the south flank of Volcán de Colima (R: Earlier intensity image, G: Later intensity image, B: Result of the later intensity image divided by the earlier intensity image) obtained from **a)** a pre-eruption image pair and **b) and c)** pre- and post-eruption image pairs. The PDC deposits appear in red (decreased surface roughness) while the lava flows at the summit appear in blue (increased surface roughness).

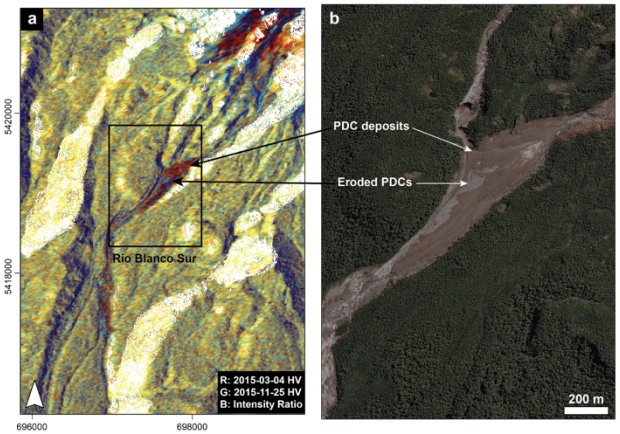

Figure 6. **a)** Georeferenced ALOS-2 false-color composite intensity ratio images of the Rio Blanco Sur valley at Volcán Calbuco (R: Earlier intensity image, G: Later intensity image, B: Result of the later intensity image divided by the earlier intensity image) obtained from a pre- and post-eruption image pair. **b)** Comparison with 0.5-m Pleiades image. The PDC deposits appear in red (decreased surface roughness) while the eroded PDCs from lahars appear in blue (increased surface roughness).

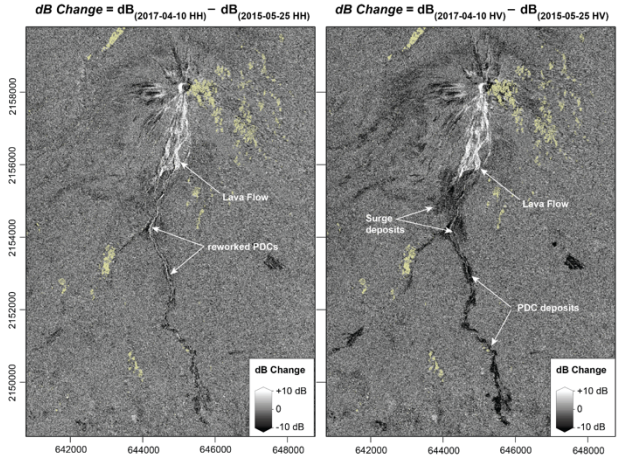

Figure 7. Georeferenced ALOS-2 Δ*dB* map of the south flank of Volcán de Colima obtained from differencing pre- and post-eruption dB images in **a)** HH-polarization and **b)** HV-polarization. Brown pixels indicate no-data values.

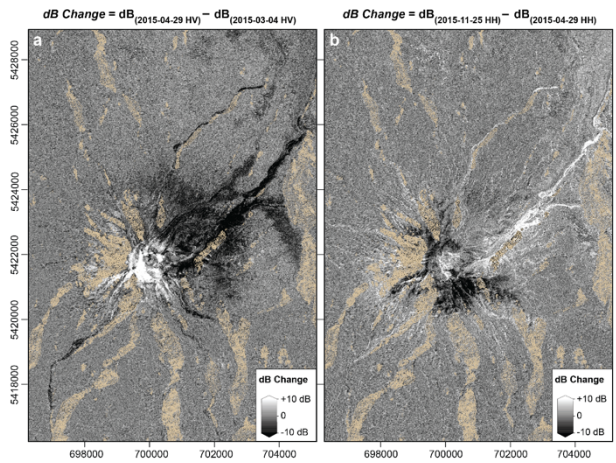

Figure 8. Georeferenced ALOS-2 Δ*dB* map of Volcán Calbuco obtained from differencing **a)** pre- and syn-eruption dB images in HV-polarization and **b)** syn- and post-eruption dB images in HH-polarization. Brown pixels indicate no-data values.

For different volcanic deposit types mapped from very high-resolution images and field data, we computed the average Δ*dB* signals (Table 1). HV polarization is more effective in displaying intensity evolution caused by the presence of volcanic deposits, while HH polarization is best suited for changes in the vegetation pattern and erosion. The Δ*dB* signal for volcanic flow deposits, either PDCs or lava flow, is about two times higher in HV than in HH polarization.

Volcano	Features	Polarization	
		HH	HV
Volcán de Colima	PDC deposits	↓ -4.2 ± 3.6 dB	↓ -8.0 ± 3.5 dB
	Ash-cloud surge deposits	↓ -1.2 ± 3.1 dB	↓ -3.9 ± 3.0 dB
	Lava flows	↑ +3.3 ± 4.6 dB	↑ +4.3 ± 4.8 dB
	Remobilized PDCs	↑ +2.5 ± 5.1 dB	↓ -0.2 ± 4.6 dB
Volcán Calbuco	PDC deposits	↓ -8.0 ± 3.3 dB	↓ -9.6 ± 3.5 dB
	Ash-cloud surge and/or tephra fall deposits	↓ -3.1± 3.3 dB	↓ -4.6 ± 3.6 dB
	Summit Changes	↑ +6.8 ± 6.4 dB	↑ +9.1 ± 6.2 dB
	Lahar erosion	↑ +7.7 ± 4.0 dB	↑ +8.0 ± 4.0 dB

Table 1. Average change in SAR intensity for individual features at Volcán de Colima and Volcán Calbuco, in co- and cross-polarization. The average intensity changes are measured in decibels (dB)

The results are comparable to other studies of PDCs mapped from SAR backscattering intensity changes at Montserrat volcano (Wadge et al., 2011), Merapi volcano in Indonesia (Solikhin et al., 2015) and Volcán de Fuego in Guatemala (Dualeh et al., 2021), which allowed us to develop "Δ*dB* signature fields" for volcanic flows (Figure 9).

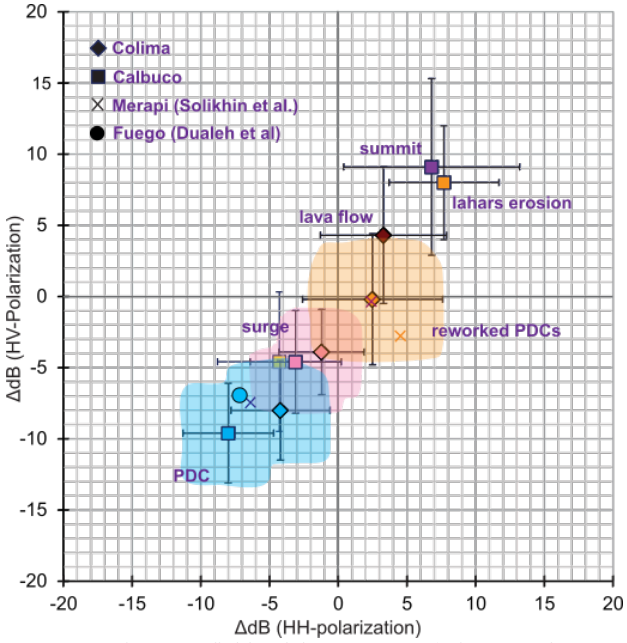

Figure 9. Signature fields of the average ΔdB in co- and cross-polarization for individual volcanic features at Volcán de Colima and Volcán Calbuco, and compared with the ΔdB measured at Merapi by Solikhin et al. (2015) and Fuego by Dualeh et al. (2021).

At Merapi volcano, Solikhin et al. (2015) also used ALOS L-band SAR backscattering intensity changes and found similar reduced surface roughness in the valleys from the deposition of PDCs, with comparable average values of ΔdB to those found at Volcán de Colima and Volcán Calbuco. At Montserrat and Volcán de Fuego, Wadge et al. (2011) and Dualeh et al. (2021) used X-band SAR basckattering intensity changes from TerraSAR-X and COSMO-SkyMed respectively. Both studies found similar results of changes in surface roughness from deposition of PDCs with an overall decrease in ΔdB.

Tracking lahars is more challenging because multiple lahars of different magnitude can occur over several days between SAR acquisitions. In the context of emergency mapping, the important information is knowing where fresh PDC deposits may become eroded and transformed into lahars during rainfall events. Finding erosional channels can provide this information. At Merapi, Solikhin et al. (2015) found increased surface roughness from reworked/eroded PDCs by lahars. They found that the higher water content resulted in $\Delta dB > 0$ in HH polarization but $\Delta dB < 0$ in HV polarization. This is consistent with findings for the reworked PDCs at Volcán de Colima, and the ΔdB values obtained by Solikhin et al. (2015) also fall within the range of the measured uncertainties. At Calbuco, however, the lahars resulted in ΔdB values closer to those measured for summit deformation. This may suggest that the changes in backscatter intensity observed cutting through the PDC deposits reflect the intense erosion, similar to what is observed at the summit, as opposed to watery reworked PDCs or lahar deposits. Dualeh et al. (2021) also found increased backscattering intensity where PDCs are being eroded by lahars. Their interpretation is that when deposits go from dry to wet, the radar penetration decreases and has more interactions with near-surface scatterers thus increasing the return signal towards the satellite. In the downstream areas of the volcanoes, the lahar deposits smooth the surface and show decreased ΔdB signals. Those results are all consistent with our findings at Volcán de Colima and Volcán Calbuco.

3.2 Probability Mapping

Probability maps (Figure 10) are generated from linear rescaling of the $|Q_{NDVI}|$ map and the SAR ΔdB map to probability values in the range [0, 1] using histogram thresholding estimated from mapping results such that:

- $P(X)_{SAR} = 0 < f(x) < 1,$

  with $f(x) = \frac{(x-\Delta dB_{min})}{(\Delta dB_{max}-\Delta dB_{min})}$ (3)

- $P(Y)_{Q_{NDVI}} = 0 < f(y) < 1,$

  with $f(y) = \frac{(x-|Q_{NDVI\_min}|)}{(|Q_{NDVI\_max}|-|Q_{NDVI\_min}|)}$ (4)

ΔdB_{min} and ΔdB_{max} are the lower and upper thresholds of intensity change for probabilities of PDC deposits between 0 and 1. For the lower threshold value for P(X) = 0, we use the average ΔdB measured for ash-cloud surge deposits in HV polarization, which is -3.5 dB. For the upper threshold value for P(X) = 1, we use the average ΔdB measured for PDC deposits in HV polarization, which is -8 dB.
$|Q_{NDVI\_min}|$ and $|Q_{NDVI\_max}|$ are the lower and upper thresholds of $|Q_{NDVI}|$ for PDC deposits set at 0.2 and 0.8 respectively.

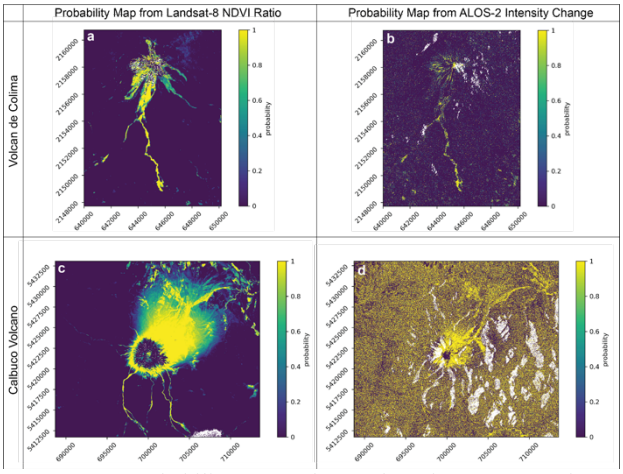

Figure 10. Probability maps of PDC deposit extent at Volcán de Colima (*top*) and Volcán Calbuco (*bottom*), from $|Q_{NDVI}|$ (**a** and **c**) and SAR ΔdB in HV polarization (**b** and **d**).

The NDVI probability map obtained with $|Q_{NDVI}|$ at Volcán de Colima (Figure 10a) shows *false positives* in the proximal area where rockfalls and lava flows were present. At Volcán Calbuco, the blanketing by tephra also covers a wider area than that of just the PDC deposits (Figure 10c). The SAR probability maps obtained with ΔdB, however, shows low probability values where lava flows were emplaced, due to the differences in ΔdB values between PDCs and lava flows (Figure 10b), but is also very noisy at Volcán Calbuco (Figure 10d). Therefore, we apply a method developed by Jo and Osmanoglu (2020) to map water flood extents by combining optical and SAR data into a weighted joint probability map. Here, the weighted joint probability algorithm is applied to combine the $|Q_{NDVI}|$ and ΔdB probability datasets to refine the mapping of PDC deposit extent (Figure 11) using Equation (5):

$$P(X|Y) = \frac{P(X)\cdot P(Y)}{P(X)\cdot P(Y)+[1-P(X)]\cdot[1-P(Y)]}, \quad (5)$$

where: P(X) = probability value on $|Q_{NDVI}|$ probability map
P(Y) = probability value on ΔdB probability map

The comparison of the histograms of the optical and SAR probability maps, with the joint probability histogram, are used here to check the performance of the technique. Background values in the $|Q_{NDVI}|$ probability map are significantly skewed towards 0, which is in agreement with the absence of any deposits. The histogram of ΔdB probability map, however, is spread over the whole range [0, 1], although with higher frequencies for lower probability values. This suggests higher background noise in the SAR probability map. Combining the results into the joint probability map is valuable to reduce the background noise and emphasize the extent of PDCs. Moreover, we find that it reduces the occurrence of *false positives* in the proximal area where lava flows and rockfalls showed as high probability pixels on the optical dataset, but with low probability values on SAR dataset.

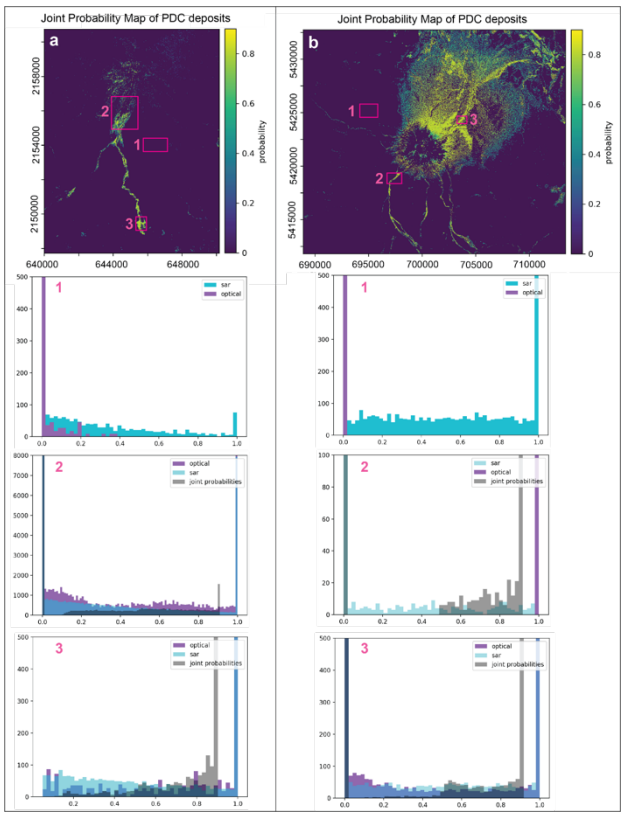

Figure 11. Joint probability maps of PDC deposit extents at **a)** Volcán de Colima and **b)** Volcán Calbuco. Histograms of the separate (optical and SAR) and joint probability maps for the areas of interests 1-3 are displayed below the respective map.

3.3 Application to the 2021 Eruption of Soufriere St Vincent

3.3.1 Soufrière St Vincent (1220 m a.s.l.), also known as "La Soufrière", is the northernmost, and youngest, stratovolcano of St Vincent and The Grenadines Island (Figure 12) located in the Lesser Antilles. Prior to 2021, its last known eruption was that of 1979 that destroyed a lava dome in the summit crater and generated several PDCs and lahars as well as tephra fall deposits and ended with the growth of a new lava dome (GVP, 2021a). After almost 42 years of quiescence, in December 2020, a new lava dome began growing SW of the 1979 dome, along with increased seismicity and gas-and-steam emissions (GVP, 2021a). Then, on April 9, 2021 La Soufrière began a series of explosive eruptions until April 22, 2021, which generated significant tephra fall deposits and numerous PDCs (GVP, 2021b). The heavy tephra fall resulted in widespread power and water outages on the island, as reported by the National Emergency Management Organization (NEMO), and some houses had collapsed due to significant ashfall. Rainfall in the following days and weeks remobilized a lot of fresh PDC and tephra deposits, generating numerous lahars (GVP, 2021b).

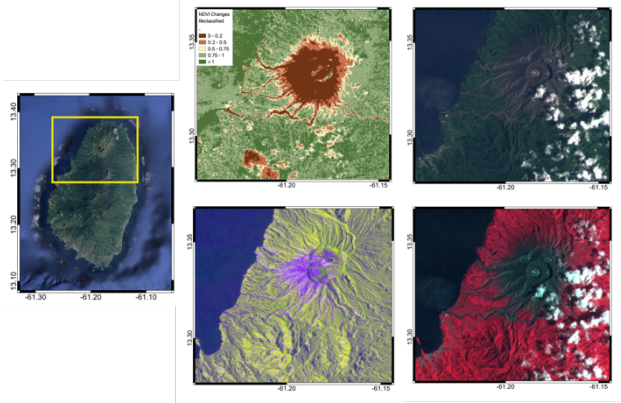

Figure 12. Soufrière St Vincent Volcano. **a)** Reclassified $|Q_{NDVI}|$ map using pre- and post-eruption Landsat-8 images showing volcanic deposits with $|Q_{NDVI}|$<0.2. **b)** False-color composite ALOS-2 ΔdB image showing the eruption products in purple from decreased SAR intensity. **c)** True color high-resolution PlanetScope image showing volcanic flows in grey going up to the sea, **d)** False-color composite PlanetScope image (R: NIR, G: Red, B: Green) showing the deposition of new volcanic products contrasting with vegetation in red.

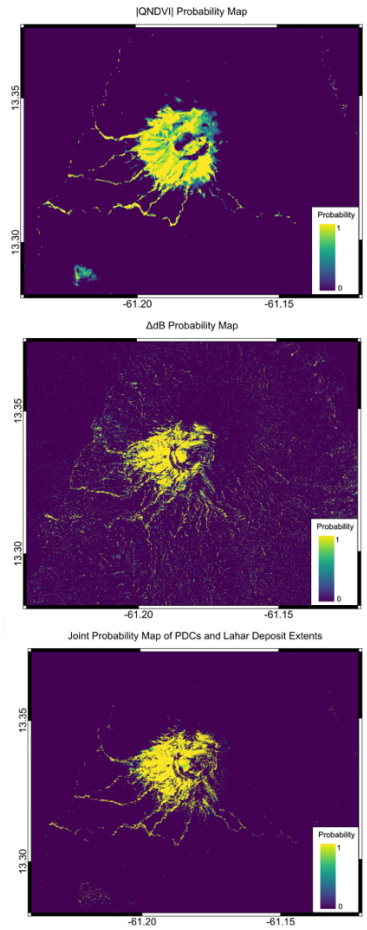

Figure 13. Probability maps at Soufrière St Vincent obtained from $|Q_{NDVI}|$ (Top) and ΔdB (Middle), and from joint probabilities (Bottom).

3.3.1 Detecting Impacted Areas Post-Eruption

Landsat and ALOS-2 images are processed and analyzed similarly to the methodology described in section 2. Using similar threshold values for ΔdB and $|Q_{NDVI}|$ changes associated with PDC deposits (Figure 12), we generate a joint probability map (Figure 13) to estimate the extent of areas impacted during the April 2021 eruption of Soufrière St Vincent.
High-resolution images from PlanetScope are used for additional analysis of volcanic flow extent and validation of areas impacted by the flows (Figure 12).
Similarly to results obtained at Volcán de Colima and Volcán Calbuco, the joint probability map of SAR backscattering intensity and optical NDVI changes allows to refine the extent of areas impacted by volcanic flows (Figure 13).

4. CONCLUSIONS

A medium-resolution mapping technique using a combination of Optical and SAR data is developed using field-based and high-resolution validation data at Volcán de Colima and Volcán Calbuco volcanoes. The technique is then successfully applied during a volcanic crisis in 2021 at Soufrière St Vincent.
This method can be tuned to better fit each volcanic crisis, and although it remains at medium-resolution, it provides tremendous potential to supporting ground-based recovery and emergency efforts.
Continuation of this work currently involves developing algorithm with Machine Learning (ML) algorithm to automate the detection of surface changes from eruption, resolved on a set of multiple optical and SAR datasets. The ML process intends to remove the need for a priori information, focusing only on dense time-series to refine the detection of volcanic flows during a volcanic crisis.
As the list of available sensors grows, we hope to continue improving the use of multi-sensor analysis to reduce data processing latency and therefore increase disaster response efficacy. Testing this methodology at different spatial and temporal-resolution can also provide pointers to what will be relevant in future spaceborne and airborne missions.

REFERENCES

Arnold, D.W.D.; Biggs, J.; Wadge, G.; Mothes, P. 2018. Using satellite radar amplitude imaging for monitoring syn-eruptive changes in surface morphology at an ice-capped stratovolcano. *Remote Sens. Environ*. 209, 480–488.

Auker, M.R.; Sparks, R.S.J.; Siebert, L.; Crosweller, H.S.; Ewert, J. 2013. A statistical analysis of the global historical volcanic fatalities record. *J. Appl. Volcanol*. 2, 1–24.

Agencia Guatemalteca de Noticias. Available online: https://agn.com.gt/gobierno-de-guatemala-erogo-3609-millones-de-quetzales-para-atender-a-victimas-de-erupcion-del-volcan-de-fuego/ (accessed on 5 June 2019).

Bignami, C., Ruch, J., Chini, M., Neri, M., Buongiorno, M. F., Hidayati, S., et al. 2013. Pyroclastic density current volume estimation after the 2010 Merapi volcano eruption using X-band SAR. *J. Volcanol. Geoth. Res*. 261, 236–243.

Boccardo P., Giulio Tonolo, F. 2014. Remote Sensing Role in Emergency Mapping for Disaster Response. Lollino, G., Manconi, A., Guzzetti, F., Culshaw, M., Bobrowsky, P., Luino, F., *Engineering Geology for Society and Territory* - Volume 5. vol. Part I, p. 17-24, ISBN: 978-3-319-09047-4

Bunting, P., Clewley, D. 2018. Atmospheric and Radiometric Correction of Satellite Imagery (ARCSI). Available online: https://github.com/remotesensinginfo/arcsi (accessed on 28 November 2019).

Dualeh, E. W., Ebmeier, S. K., Wright, T. J., Albino, F., Naismith, A., Biggs, J., et al. 2021. Analyzing explosive volcanic deposits from satellite-based radar backscatter, Volcán de Fuego, 2018. *Journal of Geophysical Research: Solid Earth*, 126, e2021JB022250.

Global Volcanism Program, 2021a. Report on Soufriere St. Vincent (Saint Vincent and the Grenadines) (Bennis, K.L., and Venzke, E., eds.). *Bulletin of the Global Volcanism Network*, 46:3. Smithsonian Institution.

Global Volcanism Program, 2021b. Report on Soufriere St. Vincent (Saint Vincent and the Grenadines) (Bennis, K.L., and Venzke, E., eds.). *Bulletin of the Global Volcanism Network*, 46:5. Smithsonian Institution.

Harris, A. J. 2015. Basaltic lava flow hazard. In *Volcanic Hazards, Risks and Disasters*, Eds: J. F. Shroder, P. Papale,17–46. Amsterdam: Elsevier.

Head, E.N., Maclean, A.L., Carn, S.A. 2012. Mapping lava flows from Nyamuragira volcano (1967-2001) with satellite data and automated classification methods. *Geomatics, Natural Hazards and Risk*, 4(2), 119-144.

Jo, M., Osmanoglu, B. 2020. Generating flood probability map based on combined use of synthetic aperture radar and optical imagery. *IGARSS 2020*.

Krippner, J.B., Belousov, A.B., Belousova, M.G., Ramsey, M.S. 2018. Parametric analysis of lava dome-collapse events and pyroclastic deposits at Shiveluch volcano, Kamchatka, using visible and infrared satellite data. *Journal of Volcanology and Geothermal Research*, 354, 115-129.

Lu, D., Mausel, P., Brondizio, E., Moran, E. 2004. Change detection techniques. *International Journal of Remote Sensing*, 25, 2365-2407.

McAlpin, D., and Meyer, F.J. 2013. Multi-sensor data fusion for remote sensing of post-eruptive deformation and depositional features at Redoubt Volcano. *Journal of Volcanology and Geothermal Research*, 259, 414-423

Macorps, E., Charbonnier, S.J., Varley, N.R., Capra, L., Atlas, Z., Cabre, J. 2018. Stratigraphy, sedimentology and inferred flow dynamics from the July 2015 block-and-ash flow deposits at Volcán de Colima, Mexico. *Journal of Volcanology and Geothermal Research*, 349, 99-116.

Macorps, E. 2021. Field and Remote Sensing Analysis of the 2015 Pyroclastic Density Currents at Colima (Mexico) and Calbuco (Chile) Volcanoes: Implications for Hazard Assessment and Crisis Management (Doctoral dissertation, University of South Florida).

Motohka, T., Isoguchi, O., Sakashita, M., Shimada, M. 2018. July. Results of ALOS-2 PALSAR-2 calibration and validation after 3 years of operation. *In IGARSS 2018 IEEE International Geoscience and Remote Sensing Symposium*, pp. 4169-4170. IEEE.

Pallister, J., Wessels, R., Griswold, J., McCausland, W., Kartadinata, N., Gunawan, H., Budianto, A., Primulyana, S. 2019. Monitoring, forecasting collapse events, and mapping pyroclastic deposits at Sinabung volcano with satellite imagery. *Journal of Volcanology and Geothermal Research*, 382, 149-163.

Poland, M. 2015. Volcano monitoring from space. *In Global Volcanic Hazards and Risk*; Loughlin, S.C., Sparks, R.S.J., Brown, S.K., Jenkins, S.F., Vye-Brown, C., Eds.; Cambridge University Press: Cambridge, UK, pp. 311–316.

Pu, R., Gong, P., Tian, Y., Miao, X., Carruthers, R.I., Anderson, G.L. 2008. Using classification and NDVI differencing methods for monitoring sparse vegetation coverage: a case study of saltcedar in Nevada, USA. *International Journal of Remote Sensing,* 29(14), 3987 — 4011.

Solikhin, A., Thouret, J-C., Gupta, A., Harris, A.J., Liew, S.C. 2012. Geology, tectonics, and the 2002-2003 eruption of the Semeru volcano, Indonesia: Interpreted from high-spatial resolution satellite imagery. *Geomorphology*, 138(1), 364-379.

Solikhin, A., Pinel, V., Vandemeulebrouck, J., Thouret, J. C., & Hendrasto, M. 2015. Mapping the 2010 Merapi pyroclastic deposits using dual-polarization Synthetic Aperture Radar (SAR) data. *Remote Sensing of Environment*, 158, 180–192.

Terunuma, T., Nishida, K., Amada, T., Mizyama, T., Sato, I., Urai, M. 2005. Detection of traces of pyroclastic flows and lahars with satellite synthetic aperture radars. *Int. J. Remote Sens.*, 26, 1927-1942.

Thouret, J-C., Gupta, A., Lube, G., Liew, S.C., Cronin, S.J., Surono, 2010. The 2006 pyroclastic deposits of Merapi Volcano, Java, Indonesia: High-spatial resolution IKONOS images and complementary ground-based observations. *Remote Sensing of Environment*, 114, 1949-1967

Valade, S., Ley, A., Massimetti, F., D’Hondt, O., Laiolo, M., Coppola, D., et al. 2019. Towards global volcano monitoring using multisensor sentinel missions and artificial intelligence: the MOUNTS monitoring system. *Remote Sens*. 11:1528.

Wadge, G., Scheuchl, B., Stevens, N.F. 2002. Spaceborne radar measurements of the eruption of Soufriere Hills Volcano, Montserrat. In, Druitt, T.H. and Kokelaar, B.P. (Eds.), The Eruption of Soufriere Hills Volcano, Montserrat, from 1995 to 1999. *Geological Society, London, Memoir*, 21, pp. 583–594.

Wadge, G.; Cole, P.; Stinton, A.; Komorowski, J.C.; Stewart, R.; Toombs, A.C.; Legendre, Y. 2011. Rapid topographic change measured by high-resolution satellite radar at Soufriere Hills Volcano, Montserrat, 2008–2010. *J. Volcanol. Geotherm. Res*. 199, 142–152

Werner, C., Wegmuller, U., Strozzi, T., Weismann, A. 2000. Gamma SAR and interferometric processing software. In *Proceedings of the ERS-ENVISAT symposium,* Gothenburg, Sweden, 1620, 1620.